Asymptotic Green's Function of a Surface Magnetic Current Element on a Perfect Electric Conductor Plane Covered by a Lossy Dielectric Substrate

Benoît Stockbroeckx and André Vander Vorst, *Fellow, IEEE*

***Abstract*— Published analyses of radiation modeling for slot structures on dielectric substrate are empirical or numerical. This paper proposes exact analytical asymptotic expressions of the far-field Green's functions of a surface magnetic current element on a perfect electric conductor plane covered by a lossy dielectric substrate of finite thickness. From these expressions, the radiation pattern of both the space wave and surface wave far away from an arbitrary shaped-slot antenna structure can be calculated, provided the source distribution across the slot is known. The potentials used in the analysis are defined and their boundary conditions are expressed. Helmholtz equation is solved in Laplace domain and the solutions are transformed into space domain using inverse Hankel transform and steepest descent method. The influences of the substrate thickness and dielectric constant are analyzed using the calculated expressions. The model is validated by comparison with surface wave and space wave measurements and with numerical results obtained from a commercial electromagnetic simulator.**

I. Introduction

PLANAR microwave hybrid circuits etched on a dielectric substrate are usually based on one of the three main topologies microstripline, slotline, and coplanar waveguide, or on a combination as single-faced or double-faced structures. The open structures radiate space and surface waves. Evaluating precisely the radiated fields becomes more and more difficult when frequency increases. The radiation source in microstrip structures is the surface electric current on the metallic strip. The radiation source in slot structures is the electric field across the slot, which can be modeled by a surface magnetic current.

Attention has been paid to slotline antennas for millimeter wave and terahertz applications [1], as well as for wide-band applications [2] where microstrip patch antennas fail [3], [4]. Experimental investigations on slot antennas [5] and design rules [6] have demonstrated the efficiency of such structures. The calculation of the radiated far fields from a given source distribution is well known in the case of a source placed at the interface between two half-spaces [7], [8]. The influence of the finite substrate height has been analyzed by several authors in the case of a hertz dipole (electric current element) [9]–[11]. The dual problem of a magnetic current element has been analyzed for multilayer configurations by using numerical [12]–[16] and analytical [17] methods. Little detail, however, is given in this last paper about the calculation. Furthermore, the final expressions of Green's functions are not given, the sensitivity to substrate thickness and dielectric constant is analyzed for very thick substrates only, the analytical results are neither validated by measurements nor compared to results from other methods, and the calculation does not take into account substrate losses, which can be very important for microwave integrated circuits on semiconductor substrates.

The aim of this paper is to derive analytically an asymptotic expression of the Green's functions for the space wave and the surface wave generated by a surface magnetic current element on a ground plane covered by a lossy dielectric substrate. The method is similar to that described in [9] so that only the steps particular to our case will be detailed. The calculation is based on an appropriate definition of potentials and specific boundary conditions to be applied. Helmholtz equation is solved for these potentials in Laplace domain and the solutions are transformed to Hankel domain to obtain Sommerfeld integrals. Their principal value are evaluated far from source by the steepest descent method and the contribution of the poles by the residue method. The influences of substrate thickness and dielectric constant on the radiation patterns are analyzed for thin and thick substrates. The calculated radiation pattern of an infinite coplanar waveguide is compared to that computed by a commercial electromagnetic simulator. The analytical model is validated by space and surface wave measurements.

II. Potentials and Boundary Conditions

The source of radiated fields is a surface current element $(\bar{\mathbf{K}}_m)$ so that the easiest way to apply boundary conditions is to solve Maxwell's equations in terms of potentials. As the current in this case is of the magnetic type, the magnetic scalar potential ϕ^f and the electric vector potential $\bar{\mathbf{F}}$ proposed by Harrington [18] are used

$$\begin{cases} \bar{\mathbf{E}} = -\nabla \times \bar{\mathbf{F}} \\ \bar{\mathbf{H}} = -j\omega\varepsilon\bar{\mathbf{F}} - \nabla\phi^f \end{cases} \tag{1}$$

with

$$\nabla \cdot \bar{\mathbf{F}} + j\omega\mu\phi^f = 0 \tag{2}$$

where $\bar{\mathbf{E}}$ is the electric field phasor and $\bar{\mathbf{H}}$ the magnetic field phasor. Helmholtz equation is obtained in terms of the electric

Manuscript received October 15, 1997.

The authors are with Laboratoire d'Hyperfréquences, Université catholique de Louvain, Bâtiment Maxwell, B-1348 Louvain-la-Neuve, Belgium.

Publisher Item Identifier S 0018-926X(99)03725-4.

vector potential

$$(\nabla^2 + k^2)\bar{\mathbf{F}} = \bar{0} \tag{3}$$

where ∇^2 is the Laplacian operator and k the wave number.

Boundary conditions applicable to the potentials ϕ^f and $\bar{\mathbf{F}}$ are not in the literature. They can be obtained by choosing realistic assumptions and integrating Maxwell's equations over infinitesimal surfaces and volumes [19]. We have shown [20] that the continuity conditions for $\bar{\mathbf{F}}$ are the following: at the interface between two dielectric media its component normal to interface is continuous, the product of the tangential component by the dielectric permittivity is continuous, and the normal gradient difference of the tangential component is compensated by the surface magnetic current $\bar{\mathbf{K}}_m$.

III. Radiated Far-Fields Calculation

The calculation is particularized here to the conductor backed dielectric slab (Fig. 1). The perfect electric conductor and dielectric substrate are supposed to be infinite in the Ox and Oy directions. Two opposite x-directed surface magnetic current elements are located on both sides of the conductor plane. They are equivalent to a y-directed electric field across an infinitesimal slot cut in the metal.

A. Solutions of Helmholtz Equation in Laplace Domain

Helmholtz equation (3) is solved in Laplace domain for the Ox-Oy plane and in the space domain for the Oz direction by defining

$$\tilde{\bar{\mathbf{F}}}(\gamma_x, \gamma_y, z) = \int_{-\infty}^{+\infty}\int_{-\infty}^{+\infty} \bar{\mathbf{F}}(x, y, z) e^{-\gamma_x x} e^{-\gamma_y y}\, dx\, dy \tag{4}$$

so that the current element expressed as a delta function in the space domain can be expressed as a constant function in Laplace domain and application of the boundary conditions becomes easier. Solutions of (3) corresponding to Fig. 1 are the following.

1) Region 1:

$$\begin{cases} \tilde{F}_x^{(1)} = -\dfrac{\varepsilon_r}{2}\dfrac{1+\tanh\left(\gamma_z^{(2)}d\right)}{D} K_m e^{-\gamma_z^{(2)}d} e^{-\gamma_z^{(1)}(z-d)} \\ \tilde{F}_z^{(1)} = \dfrac{\gamma_x}{2}\dfrac{(1-\varepsilon_r)\left[1+\tanh\left(\gamma_z^{(2)}d\right)\right]}{BD} K_m e^{-\gamma_z^{(2)}d} e^{-\gamma_z^{(1)}(z-d)} \end{cases} \tag{5}$$

2) Region 2: [See (6) at the bottom of the page.]

3) Region 3:

$$\tilde{F}_x^{(3)} = \frac{K_m}{2\gamma_z^{(1)}} e^{\gamma_z^{(1)} z} \tag{7}$$

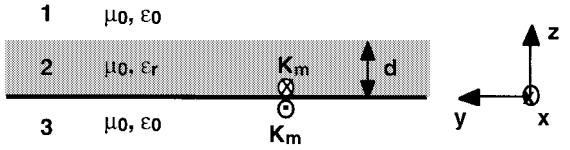

Fig. 1. x-oriented surface magnetic current elements equivalent to elementary y-oriented electric field for slot radiation analysis: (1) air, (2) dielectric slab, (3) air. Perfect electric conductor between (2) and (3).

with

$$\gamma_z^{(1)} = j\sqrt{\gamma_x^2 + \gamma_y^2 + k_0^2}, \quad \gamma_z^{(2)} = j\sqrt{\gamma_x^2 + \gamma_y^2 + \varepsilon_r k_0^2}$$

$$D = \varepsilon_r \gamma_z^{(1)} + \gamma_z^{(2)} \tanh\left(\gamma_z^{(2)} d\right) \tag{8}$$

$$B = \gamma_z^{(1)} + \gamma_z^{(2)} \coth\left(\gamma_z^{(2)} d\right). \tag{9}$$

The x-oriented surface magnetic current element yields the x component of the potential, the interface between air and dielectric yields the z component, and there is no y component. The zeros of denominators D (8) and B (9) correspond to TM and TE surface waves, respectively.

B. Inverse Laplace Transform and Hankel Transform

Solutions (5) to (7) can be expressed in space domain by calculating the inverse Laplace transform defined as

$$\bar{\mathbf{F}}(x, y, z) = \frac{1}{(2\pi)^2}\int_{c-j\infty}^{c+j\infty}\int_{c'-j\infty}^{c'+j\infty} \tilde{\bar{\mathbf{F}}}(\gamma_x, \gamma_y, z) e^{\gamma_x x} e^{\gamma_y y}\, d\gamma_x\, d\gamma_y. \tag{10}$$

Changing variables by defining [21] $x + jy = \rho e^{j\varphi}$ and $\gamma_x + j\gamma_y = \gamma_\rho e^{j\psi}$ yields $\bar{\mathbf{F}}(x, y, z) \rightarrow \bar{\mathbf{U}}(\rho, \varphi, z)$ and $\tilde{\bar{\mathbf{F}}}(\gamma_x, \gamma_y, z) \rightarrow \tilde{\bar{\mathbf{U}}}(\gamma_\rho, \psi, z)$, where ρ and φ are standard polar coordinates and γ_ρ and ψ complex numbers. Integrals (10) become

$$\bar{\mathbf{U}}(\rho, \varphi, z) = \frac{1}{(2\pi)^2}\int_{C''}\int_{C'} \tilde{\bar{\mathbf{U}}}(\gamma_\rho, \psi, z) e^{\gamma_\rho \rho \cos(\psi - \varphi)} \gamma_\rho\, d\gamma_\rho\, d\psi \tag{11}$$

The integral representation of Hankel function $H_n^{(2)}(z)$ given by [22] can be easily transformed into

$$H_n^{(2)}(z) = \frac{1}{\pi}\int_{\frac{\pi}{2}-j\infty}^{\frac{3\pi}{2}+j\infty} e^{jz\cos(t) - jn\left(\frac{\pi}{2} - t\right)}\, dt \tag{12}$$

By choosing the same integration path for C'' in the complex plane ψ in (11) as in (12) [23], putting

$$\tilde{\bar{\mathbf{U}}}(\gamma_\rho, \psi, z) = \frac{1}{\pi}\tilde{\bar{\chi}}_n(\gamma_\rho, z) e^{-jn\frac{\pi}{2}} e^{jn\psi} \tag{13}$$

$$\begin{cases} \tilde{F}_x^{(2)} = -\dfrac{K_m}{4\gamma_z^{(2)} D\cosh\left(\gamma_z^{(2)}d\right)}\left[\left(\gamma_z^{(2)} - \varepsilon_r\gamma_z^{(1)}\right)e^{-\gamma_z^{(2)}d} e^{\gamma_z^{(2)}z} + \left(\gamma_z^{(2)} + \varepsilon_r\gamma_z^{(1)}\right)e^{\gamma_z^{(2)}d} e^{-\gamma_z^{(2)}z}\right] \\ \tilde{F}_z^{(2)} = \dfrac{\gamma_x}{2}\dfrac{(1-\varepsilon_r)\left[1+\tanh\left(\gamma_z^{(2)}d\right)\right]}{BD\sinh\left(\gamma_z^{(2)}d\right)} K_m e^{-\gamma_z^{(2)}d}\sinh\left(\gamma_z^{(2)}z\right) \end{cases} \tag{6}$$

and taking (12) into account, (11) is transformed into

$$\bar{\mathbf{U}}(\rho,\varphi,z)=\frac{1}{(2\pi)^2}\int_{C'}\gamma_\rho\tilde{\tilde{\chi}}_n(\gamma_\rho,z)e^{jn\varphi}H_n^{(2)}\left(\frac{\gamma_\rho\rho}{j}\right)d\gamma_\rho. \tag{14}$$

Integral (14) is the inverse Hankel transform of $\tilde{\tilde{\chi}}_n(\gamma_\rho,z)$ [21] and is known as Sommerfeld integral [9], [24].

C. Asymptotic Evaluation of Sommerfeld Integral

The evaluation of (14) is explained in [9] and will only be outlined here. Integral (14) is of the following form:

$$S_n[fe^{-\gamma_z z}]=\int_{C'}\gamma_\rho^{n+1}H_n^{(2)}\left(\frac{\gamma_\rho\rho}{j}\right)f(\gamma_\rho)e^{-\gamma_z z}\,d\gamma_\rho. \tag{15}$$

The value of the integral is the sum of two terms: the principal value and the pole contribution. It is supposed here that only TM_0 surface wave propagates so that only one pole is exhibited by the function f at $\gamma_\rho=\gamma_p$, where γ_p is the propagation exponent of the TM_0 surface wave mode. The principal value is obtained by an integration method, which is known as either steepest descent or saddle-point method [25]. It can be shown that the integrand in (15) has a saddle point. If the integration path C' is modified so that the steepest descent path is followed, then this path has that saddle point as a maximum. The principal value of integral (15) is consequently determined by the value of its integrand at the saddle point. The contribution of the pole is obtained by the residue method.

By introducing the spherical coordinate system (r,θ,φ), for elevation angles such that $\theta>\theta_p\triangleq\arcsin(\frac{jk_0}{\gamma_p})$, the pole in the integrand has no effect and (15) is given by its principal value which results in a space wave. For small elevation angles $\theta<\theta_p$ the contribution of the pole has to be added to the principal value. The asymptotic expression of integral (15) is then given by

$$\begin{aligned}S_n[fe^{-\gamma_z z}]&\cong 2j^{2n+3}\cos(\theta)k_0^{n+1}(\sin\theta)^n f(jk_0\sin\theta)\frac{e^{-jk_0r}}{r}\\&\quad+U(\theta-\theta_p)2\pi jR(\gamma_p)\gamma_p^{n+1}H_n^{(2)}\left(\frac{\gamma_\rho\rho}{j}\right)\\&\quad e^{-j\sqrt{\gamma_p^2+\varepsilon_r k_0^2}z}\end{aligned} \tag{16}$$

where U is the unit step function and $R(\gamma_p)$ is the residue of $f(\gamma_\rho)$ at $\gamma_\rho=\gamma_p$.

The pole γ_p is the solution of the transcendental equation $D=0$ (8). The residue $R(\gamma_p)$ is very sensitive to the value of the pole, which, hence, has to be determined very precisely. We compute it using an original variational formulation [26], [27]. The electric vector potential (5)–(7) can then be expressed in space domain by using (11), (13), (14), (16). The electromagnetic fields can be calculated by using (1), (2). They are expressed using Green's formulation in the three regions.

The space wave is given by the following.

1) Region 1

$$\begin{cases}\begin{pmatrix}E_\theta\\E_\varphi\end{pmatrix}=\begin{pmatrix}G_{e1}^{(1)}(\theta,\varphi) & G_{e1}^{(1)}(\theta,\varphi-\frac{\pi}{2})\\ G_{e2}^{(1)}(\theta,\varphi) & G_{e2}^{(1)}(\theta,\varphi-\frac{\pi}{2})\end{pmatrix}\begin{pmatrix}K_{mx}\\K_{my}\end{pmatrix}\frac{e^{-jk_0r}}{r}\\ \begin{pmatrix}H_\theta\\H_\varphi\end{pmatrix}=\begin{pmatrix}G_{h1}^{(1)}(\theta,\varphi) & G_{h1}^{(1)}(\theta,\varphi-\frac{\pi}{2})\\ G_{h2}^{(1)}(\theta,\varphi) & G_{h2}^{(1)}(\theta,\varphi-\frac{\pi}{2})\end{pmatrix}\begin{pmatrix}K_{mx}\\K_{my}\end{pmatrix}\frac{e^{-jk_0r}}{r}\\ E_r=H_r=0.\end{cases} \tag{17}$$

2) Region 3:

$$\begin{cases}\begin{pmatrix}E_\theta\\E_\varphi\end{pmatrix}=\begin{pmatrix}G_{e1}^{(3)}(\theta,\varphi) & G_{e1}^{(3)}(\theta,\varphi-\frac{\pi}{2})\\ G_{e2}^{(3)}(\theta,\varphi) & G_{e2}^{(3)}(\theta,\varphi-\frac{\pi}{2})\end{pmatrix}\begin{pmatrix}K_{mx}\\K_{my}\end{pmatrix}\frac{e^{-jk_0r}}{r}\\ \begin{pmatrix}H_\theta\\H_\varphi\end{pmatrix}=\begin{pmatrix}G_{h1}^{(3)}(\theta,\varphi) & G_{h1}^{(3)}(\theta,\varphi-\frac{\pi}{2})\\ G_{h2}^{(3)}(\theta,\varphi) & G_{h2}^{(3)}(\theta,\varphi-\frac{\pi}{2})\end{pmatrix}\begin{pmatrix}K_{mx}\\K_{my}\end{pmatrix}\frac{e^{-jk_0r}}{r}\\ E_r=H_r=0\end{cases} \tag{18}$$

with

$$\begin{aligned}G_{e1}^{(1)}&=jk_0\frac{\varepsilon_r}{4\pi}\sin\varphi\frac{\cos\theta}{D_1\cosh(jk_0Td)}e^{jk_0d\cos\theta}\\ G_{e2}^{(1)}&=jk_0\frac{1}{4\pi}\cos\varphi\frac{NT\cos\theta}{D_1D_2\cosh(jk_0Td)}e^{jk_0d\cos\theta}\\ G_{h1}^{(1)}&=-j\omega\frac{\varepsilon_0}{4\pi}\cos\varphi\frac{NT\cos\theta}{D_1D_2\cosh(jk_0Td)}e^{jk_0d\cos\theta}\\ G_{h2}^{(1)}&=j\omega\frac{\varepsilon_0\varepsilon_r}{4\pi}\sin\varphi\frac{\cos\theta}{D_1\cosh(jk_0Td)}e^{jk_0d\cos\theta}\\ G_{e1}^{(3)}&=-jk_0\frac{1}{4\pi}\sin\varphi\\ G_{e2}^{(3)}&=-jk_0\frac{1}{4\pi}\cos\varphi\cos\theta\\ G_{h1}^{(3)}&=j\omega\frac{\varepsilon_0}{4\pi}\cos\varphi\cos\theta\\ G_{h2}^{(3)}&=-j\omega\frac{\varepsilon_0}{4\pi}\sin\varphi.\end{aligned}$$

The surface wave is given by the following.

1) Region 1: [See (19) at the bottom of the next page.]

2) Region 2:

$$\begin{cases}\begin{pmatrix}E_\rho\\E_z\end{pmatrix}=\begin{pmatrix}G_{e3}^{(2)}(\varphi) & G_{e3}^{(2)}(\varphi-\frac{\pi}{2})\\ G_{e4}^{(2)}(\varphi) & G_{e4}^{(2)}(\varphi-\frac{\pi}{2})\end{pmatrix}\begin{pmatrix}K_{mx}\\K_{my}\end{pmatrix}\frac{e^{-\gamma_p\rho}}{\sqrt{\rho}}\\ H_\varphi=\begin{pmatrix}G_{h3}^{(2)}(\varphi) & G_{h3}^{(2)}(\varphi-\frac{\pi}{2})\end{pmatrix}\begin{pmatrix}K_{mx}\\K_{my}\end{pmatrix}\frac{e^{-\gamma_p\rho}}{\sqrt{\rho}}\\ E_\varphi=H_\rho=H_z=0\end{cases} \tag{20}$$

with

$$\begin{aligned}G_{e3}^{(1)}&=-\frac{\varepsilon_r}{4}\gamma_{zp}^{(1)}\sin\varphi\frac{R_D}{\cosh(\gamma_{zp}^{(2)}d)}\sqrt{\frac{2\gamma_p}{\pi}}\\ G_{e4}^{(1)}&=\frac{\varepsilon_r}{4}\gamma_p\sin\varphi\frac{R_D}{\cosh(\gamma_{zp}^{(2)}d)}\sqrt{\frac{2\gamma_p}{\pi}}\\ G_{h3}^{(1)}&=-j\omega\frac{\varepsilon_0\varepsilon_r}{4}\sin\varphi\frac{R_D}{\cosh(\gamma_{zp}^{(2)}d)}\sqrt{\frac{2\gamma_p}{\pi}}\end{aligned}$$

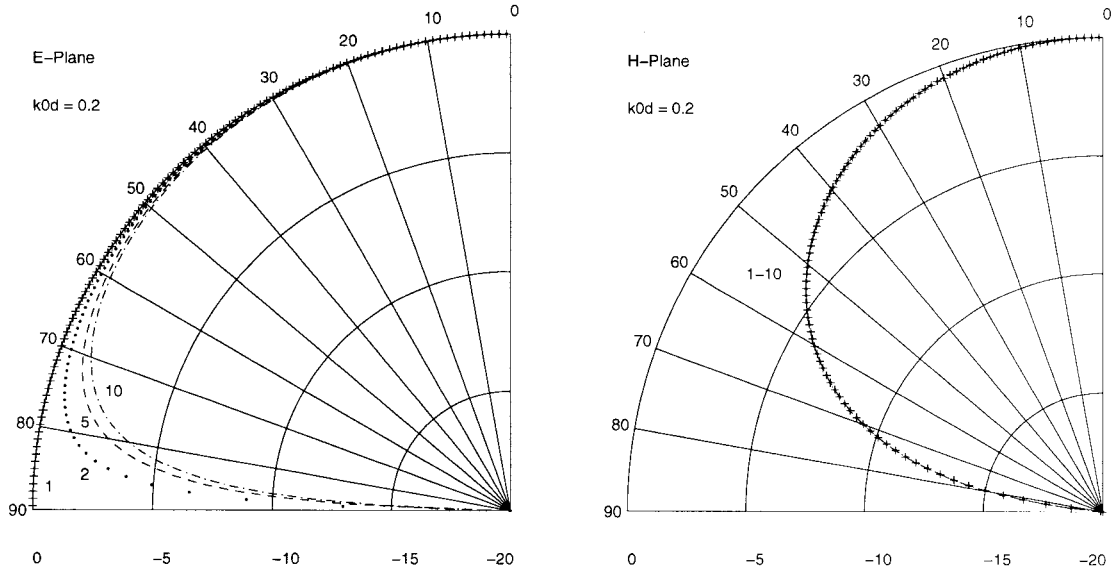

Fig. 2. Sensitivity of space wave Green's function in Region 1 to dielectric permittivity in E plane ($\varphi = \pi/2$) (a) and in H plane ($\varphi = 0$) (b); $\varepsilon_r = 1$ (+), 2 (.), 5 (--), and 10 (-.); for thin substrate ($k_0 d = 0.2$).

$$
\begin{aligned}
G_{e3}^{(2)} &= \frac{1}{4}\sin\varphi \frac{R_D}{\cosh\left(\gamma_{zp}^{(2)} d\right)} \sqrt{\frac{2\gamma_p}{\pi}} \\
&\quad \times \left\{-\varepsilon_r \gamma_{zp}^{(1)} \cosh\left[\gamma_{zp}^{(2)}(z-d)\right] \right. \\
&\quad \left. + \gamma_{zp}^{(2)} \sinh\left[\gamma_{zp}^{(2)}(z-d)\right]\right\} \\
G_{e4}^{(2)} &= \frac{1}{4}\sin\varphi \frac{R_D}{\gamma_{zp}^{(2)} \cosh\left(\gamma_{zp}^{(2)} d\right)} \gamma_p \sqrt{\frac{2\gamma_p}{\pi}} \\
&\quad \times \left\{\gamma_{zp}^{(2)} \cosh\left[\gamma_{zp}^{(2)}(z-d)\right] \right. \\
&\quad \left. - \varepsilon_r \gamma_{zp}^{(1)} \sinh\left[\gamma_{zp}^{(2)}(z-d)\right]\right\} \\
G_{h3}^{(2)} &= -j\omega \frac{\varepsilon_0 \varepsilon_r}{4}\sin\varphi \frac{R_D}{\gamma_{zp}^{(2)} \cosh\left(\gamma_{zp}^{(2)} d\right)} \sqrt{\frac{2\gamma_p}{\pi}} \\
&\quad \times \left\{\gamma_{zp}^{(2)} \cosh\left[\gamma_{zp}^{(2)}(z-d)\right] \right. \\
&\quad \left. - \varepsilon_r \gamma_{zp}^{(1)} \sinh\left[\gamma_{zp}^{(2)}(z-d)\right]\right\} \\
\gamma_{zp}^{(1)} &= j\sqrt{\gamma_p^2 + k_0^2}; \quad \gamma_{zp}^{(2)} = j\sqrt{\gamma_p^2 + \varepsilon_r k_0^2} \\
R_D &= \frac{1}{\gamma_p} \frac{\gamma_{zp}^{(2)^2} \gamma_{zp}^{(1)} \left[\cosh\left(\gamma_{zp}^{(2)} d\right)\right]^2}{k_0^2 \varepsilon_r (\varepsilon_r - 1)\left[\cosh\left(\gamma_{zp}^{(2)} d\right)\right]^2 - d\gamma_{zp}^{(2)^2} \gamma_{zp}^{(1)}} \\
T &= \sqrt{\varepsilon_r - (\sin\theta)^2} \\
D_1 &= \varepsilon_r \cos\theta + T \tanh(jk_0 T d); \\
D_2 &= \cos\theta + T \coth(jk_0 T d) \\
N &= T + \varepsilon_r \cos\theta \coth(jk_0 T d).
\end{aligned}
$$

Analytical expressions (17)–(20) are exact for far fields. This is the original result of the present paper. Our analytical method can be extended to multilayered configurations.

IV. Sensitivity of the Green's Functions to Substrate Thickness and Dielectric Constant

Green's function expressions (17)–(20) are rather complicated and, in particular, the influence of the substrate physical parameters is not obvious. It is, therefore, interesting to obtain a qualitative idea of the sensitivity of those expressions to substrate thickness and dielectric constant by some numerical examples. Figs. 2 and 3 depict this influence in the E ($\varphi = \pi/2$) and H ($\varphi = 0$) planes for the space wave in Region 1, for thin and thick substrates, respectively, and for $\varepsilon_r = 1, 2, 5$, and 10. The sensitivity to dielectric permittivity is more significant in the E plane than in the H plane for a thin substrate (Fig. 2): the relative power density at 80° changes from 0 dB to −4 dB in the E plane for an ε_r changing from one to ten, while there is no change in the H plane. The sensitivity is as significant in the E plane as in the H plane for a thick substrate (Fig. 3): the direction of the radiation maximum changes from 0° to 65° in both planes, the −3 dB aperture changes from 65° to 90° in the E plane and from 45° to 82° in the H plane. It is observed that the influence of the dielectric permittivity is not monotonic for a thick substrate (Fig. 3): the −3 dB aperture for $\varepsilon_r = 5$ is larger than those for $\varepsilon_r = 2$ and 10 in the H plane. The same conclusion is found in [9] for the radiation pattern of an electric current element.

V. Comparison and Validation

A. Validation with Surface Wave Measurements

Expressions (20) of the surface wave radiation pattern are compared with measurements. Surface wave measurement is a

$$
\begin{cases}
\begin{pmatrix} E_\rho \\ E_z \end{pmatrix} = \begin{pmatrix} G_{e3}^{(1)}(\varphi) & G_{e3}^{(1)}\left(\varphi - \frac{\pi}{2}\right) \\ G_{e4}^{(1)}(\varphi) & G_{e4}^{(1)}\left(\varphi - \frac{\pi}{2}\right) \end{pmatrix} \begin{pmatrix} K_{mx} \\ K_{my} \end{pmatrix} e^{-\gamma_{zp}^{(1)}(z-d)} \dfrac{e^{-\gamma_p \rho}}{\sqrt{\rho}} \\
H_\varphi = \left(G_{h3}^{(1)}(\varphi) \quad G_{h3}^{(1)}\left(\varphi - \frac{\pi}{2}\right)\right) \begin{pmatrix} K_{mx} \\ K_{my} \end{pmatrix} e^{-\gamma_{zp}^{(1)}(z-d)} \dfrac{e^{-\gamma_p \rho}}{\sqrt{\rho}} \\
E_\varphi = H_\rho = H_z = 0.
\end{cases} \tag{19}
$$

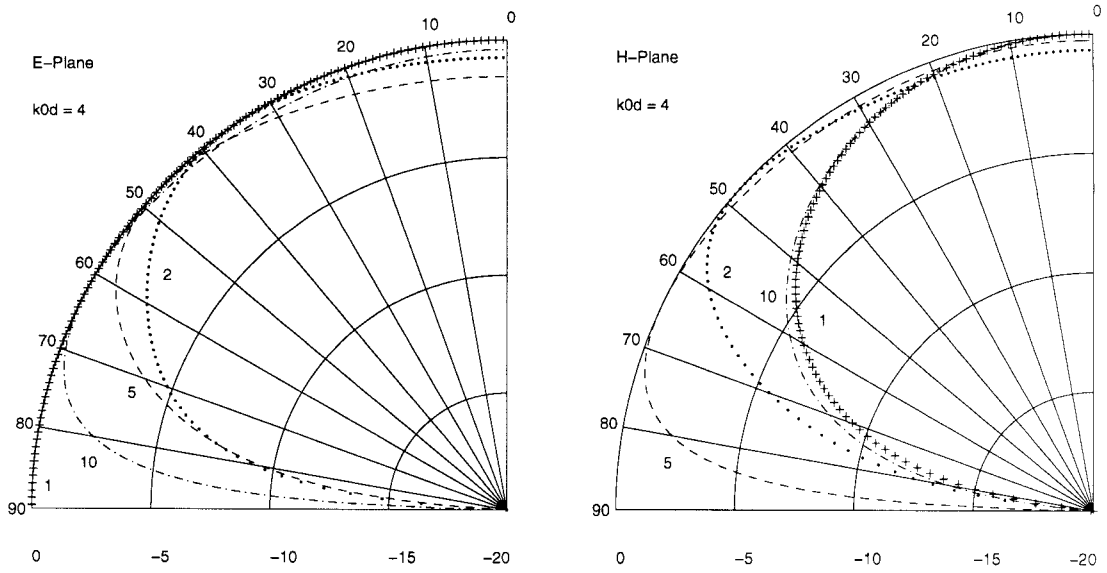

Fig. 3. Sensitivity of space wave Green's function in Region 1 to dielectric permittivity in E plane ($\varphi = \pi/2$) (a), and in H plane ($\varphi = 0$) (b); $\varepsilon_r = 1$ (+), 2 (.), 5 (--), and 10 (-.); for thick substrate ($k_0 d = 4$).

delicate operation due to the high number of parasitic effects to be cancelled: parasitic radiations, cross-polar radiation, multiple reflections, probe perturbation, and low signal levels.

The purpose is to validate the radiation pattern of an infinitesimal surface magnetic current element (element factor). Meanwhile the measured pattern is the product of this element factor by the array factor of the source. Consequently, the latter must have no zero. Moreover, the aperture constituting the source must be fed without parasitic radiation. The chosen solution is a small rectangular aperture fed by the TE_{10} dominant mode of a rectangular waveguide. The transition does not radiate and the aperture can be very small.

The TM_0 surface wave consists of three field components: E_ρ, E_z, and H_φ. A good way for detecting them is to make use of a radial microstrip probe, because its dominant mode will match perfectly with E_z and H_φ. The measurement structure is depicted in Fig. 4. The WR-42 rectangular waveguide soldered to the conductor plane is fed by a coax-to-waveguide transition connected with a network analyzer. There are five 50 Ω microstrip line probes, at azimuthal angles $\varphi = 0°, 23°, 45°, 68°$, and $90°$, respectively, matched with the coaxial cables of the network analyzer. Hence, there are no radiating standing waves on the lines. Triangle-shaped Ecosorb ferrite absorbers are placed to avoid multiple reflections of surface waves at the slab edges. They are 1.25-mm thick and the material is optimized for a working frequency of 24 GHz. The dielectric substrate has been chosen so that the first higher surface wave mode cannot propagate at 24 GHz; relative permittivity is 11.4 and thickness is 0.635 mm. The radiating source is a rectangular slot ($L = 4.32$ mm, $W = 2$ mm) fed by a K-band rectangular waveguide. The 50 Ω microstrip width is $W_{\text{mic}} = 0.657$ mm and the radial distance between the center of the aperture and the nearest end of the microstrip lines is $R = 20$ mm. This circuit is etched on a large 100 mm $\times$ 100 mm square wafer to minimize the effect of multiple reflections.

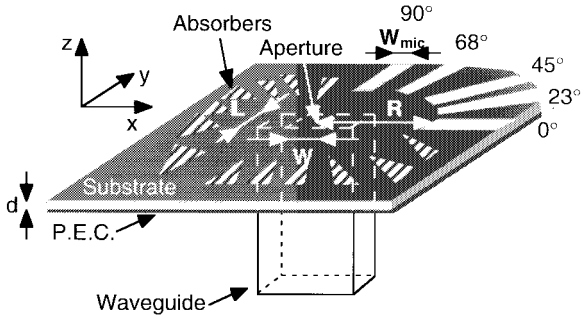

Fig. 4. Surface wave measurement structure.

The electric field in the aperture is supposed to be y oriented and uniformly distributed. The array factor corresponding to the aperture is plotted in Fig. 5. It has no zero so that it can be inverted and the element factor can be obtained.

The transmission is measured with a Wiltron 360B vector analyzer over the full waveguide bandwidth (18–26.5 GHz). The standard coaxial method is used for calibration since absolute transmission levels are not necessary; only relative levels indeed between the five transmission measurements are needed. The measured transmission coefficients are plotted in Fig. 6 for the five directions 90°, 68°, 45°, 23°, and 0°, as well as the noise level measured without feeding the aperture. It is observed that the measured levels are globally ordered with a decreasing transmission level for a decreasing azimuthal angle φ. This ordering is not exact for some frequency points due to several reasons: the aperture has not been matched to the waveguide, the coax- to-waveguide and coax-to-microstrip line transitions have not the same transmission coefficient at every frequency, and the multiple reflections are not totally cancelled. The transmission at 0° cannot be distinguished from the noise at the lowest frequencies of the band.

The surface wave radiation pattern is obtained by normalizing the measured transmission coefficients in the four

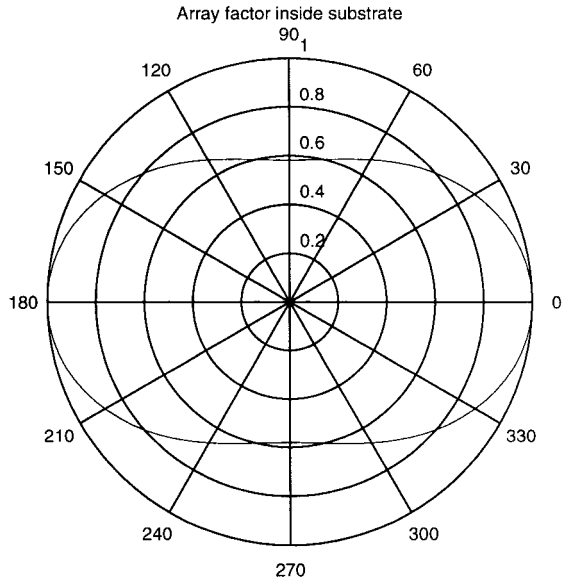

Fig. 5. Simulated array factor of rectangular source aperture versus polar angle φ.

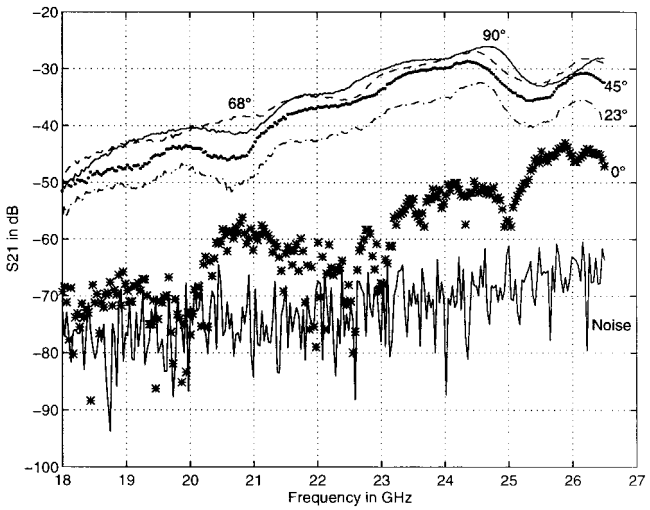

Fig. 6. Transmission coefficients measured between coaxial cables connected to waveguide feeder and microstrip lines at $\varphi = 90°$ (-), $68°$ (--), $45°$ (.), $23°$ (-.), $0°$ (*); noise measured without feeding the aperture (-).

directions ($\varphi = 68°, 45°, 23°$, and $0°$) with respect to the measured transmission coefficient for $\varphi = 90°$. It is plotted in Fig. 7. The reference at 90° is indicated by the star (0 dB) and the patterns for the other four directions are given by the dots, each dot corresponding to one frequency point. The simulated radiation pattern is plotted on the same graph for the two frequency limits of the measurement bandwidth (18 GHz and 26.5 GHz). In the directions $\varphi = 68°, 45°$ and $23°$, the measured dots are centered and more concentrated around the two simulated lines which indicates a good agreement. In the direction $\varphi = 0°$, the simulated curves vanish and the dots are below -10 dB, so that the low transmission level is confirmed. This nonzero transmission coefficient in the direction $\varphi = 0°$ can be caused by several mechanisms: reflections off the other microstrip probes, absorbers, slab edges, or cross-polar radiation due to a not predicted x component of the electric

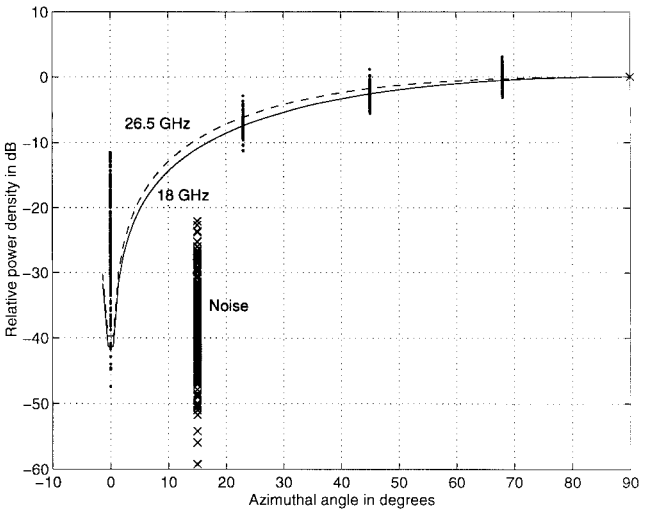

Fig. 7. Simulated surface wave radiation patterns at 18 GHz (-) and 26.5 GHz (- -); measured surface wave radiation pattern in K-band(.); noise level (x).

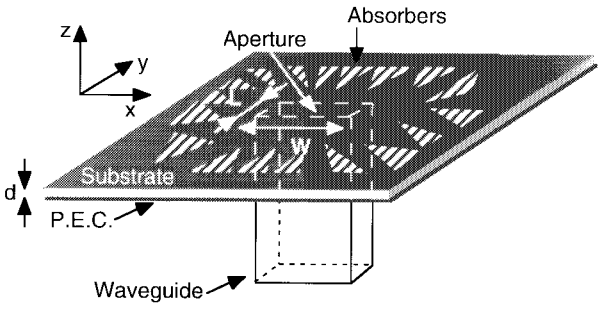

Fig. 8. Space wave measurement structure.

field source in the aperture (the dominant y component has only been taken into account). Moreover, a large part of the dots at 0° are below the noise level represented by the crosses in Fig. 7. The surface wave radiation pattern modeling is consequently valid in spite of the measurement spread.

B. Validation with Space Wave Measurements

Equation (17) of the space wave radiation pattern are compared to measurements. Space wave radiation pattern measurements are not easy to perform due to the diffraction on the edges of the structure, which is obviously not infinite. The purpose is to validate the radiation pattern of an infinitesimal surface magnetic current element. The constraints on the source are the same as for surface wave measurements. The radiating source is consequently the same.

The measurement structure is depicted in Fig. 8. The WR-42 rectangular waveguide soldered to the conductor plane is fed by a Gunn diode cell at 24.125 GHz. The dielectric substrate is characterized by its relative permittivity (11.4) and thickness (0.635 mm). A K-band rectangular waveguide is the feeder, with as aperture dimensions $L = 4.32$ mm, $W = 10.67$ mm. Surface waves have to be absorbed to avoid parasitic radiation at the edges of the wafer and absorbers have been glued on

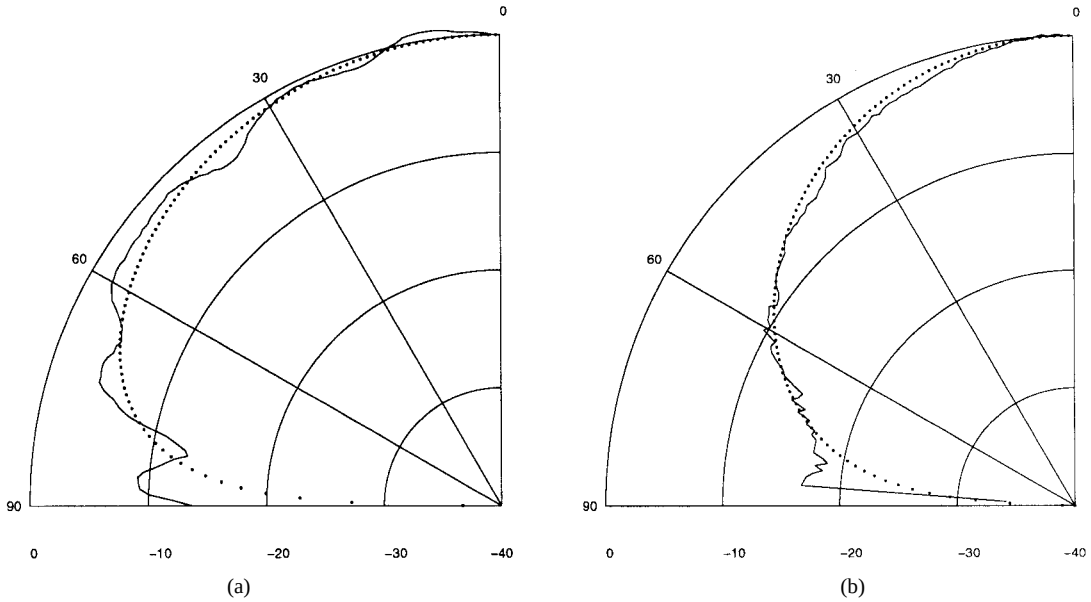

Fig. 9. Comparison between measured (-) and simulated (.) space wave radiation patterns in (a) E and (b) H planes.

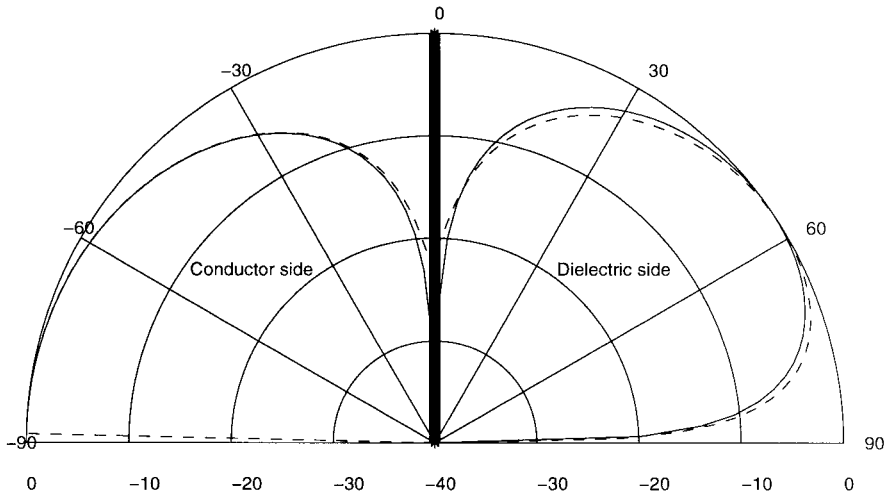

Fig. 10. Space wave radiation patterns in E plane of coplanar waveguide; comparison between analytical model (-) and numerical simulation from IE-3D software (- -) on conductor side and dielectric side.

the dielectric substrate for this purpose. The wafer is a 15 cm $\times$ 15 cm square.

The radiation patterns in the E and H planes, $\varphi = 90°$ and $0°$, respectively, have been measured with a parabolic antenna in an anechoic chamber. Simulated and measured patterns in the E and H planes are compared in Fig. 9. The measured pattern in the E plane exhibits some ripple due to the residual diffraction at the edges of the structure. The correspondence between simulations and measurements in the E and H planes is globally good, except for grazing angles where residual diffraction and residual surface wave cause sidelobes rather than zeros.

C. Comparison with Numerical Results from IE-3D Simulator

The measurements are perturbed at grazing angles by parasitic diffraction (Fig. 9). As the influence of the substrate is visible and has to be validated for such angles (Figs. 2 and 3), a comparison has been performed between the results of our model and these obtained from a commercial software, the IE-3D electromagnetic simulator from Zealand Software.

The structure under test for this comparison is an infinite coplanar waveguide. Its slot width is 1 mm and central conductor width is 2 mm. It is etched on a dielectric substrate 0.635 mm thick with $\varepsilon_r = 10.8$. The radiation is simulated at 24.125 GHz in the E plane, perpendicular to the transmission line on both conductor and dielectric sides. The comparison is plotted in Fig. 10. The most important results are on the dielectric side: the two simulated patterns agree very well. The comparison between the effect of the dielectric substrate obtained by the analytical model and by the numerical simulation shows a very good agreement. The two simulated radiation patterns on the conductor side agree very well too.

As the commercial software is known to compute accurate radiation patterns, the comparison in Fig. 10 is convincing enough to prove the accuracy of the analytical model.

VI. Conclusion

Analytical asymptotic expressions of the Green's functions of a surface magnetic current element on a ground plane covered by a lossy dielectric substrate have been derived by defining appropriate electromagnetic potentials and associated boundary conditions. The derivation uses Hankel transform, steepest descent, and residue methods. These analytical expressions are original. The sensitivity of the calculated Green's functions to the substrate thickness and dielectric constant in the E and H planes has been investigated for thin and thick substrates. The E-plane is more sensitive to the dielectric permittivity for a thin substrate than the H plane, while both E and H planes are sensitive for a thick substrate. The influence of the dielectric constant in the radiation pattern of the magnetic current is not monotonic. The analytical model has been validated by comparison with space wave and surface wave measurements and by comparison with the computed results obtained from a commercial electromagnetic simulator. The method can be extended to multilayered configurations.

Acknowledgment

The authors would like to thank R. Platteborze, P. Vanaverbeke, and the staff of BER s.a., Belgium, for their helpful assistance in setting up the measurement equipment.

References

[1] G. M. Rebeiz, "Millimeter-wave and terahertz integrated circuit antennas," *Proc. IEEE*, vol. 80, pp. 1748–1770, Nov. 1992.
[2] J. Chramiec, H. Aubert, and H. Baudrand, "Application of bilateral slotlines to broadband microwave components," in *Proc. 23rd Eur. Microwave Conf.*, Madrid, Spain, 1993, pp. 577–580.
[3] H. S. Tsai, M. J. W. Rodwell, and R. A. York, "Planar amplifier array with improved bandwidth using folded-slots," *IEEE Microwave Guided Wave Lett.*, vol. 4, pp. 112–114, Apr. 1994.
[4] H. S. Tsai and R. A. York, "Polarization-rotating quasi-optical reflection amplifier cell," *Electron. Lett.*, vol. 29, pp. 2125–2127, Nov. 1993.
[5] Y. Yoshimura, "A microstripline slot antenna," *IEEE Trans. Microwave Theory Tech.*, vol. 20, pp. 760–762, Nov. 1972.
[6] H. S. Tsai and R. A. York, "Multislot 50-Ω antennas for quasi-optical circuits," *IEEE Trans. Microwave Guided Wave Lett.*, vol. 5, pp. 180–182, June 1995.
[7] M. Kominami, D. M. Pozar, and D. H. Schaubert, "Dipole and slot elements and arrays on semi-infinite substrates," *IEEE Trans. Antennas Propagat.*, vol. AP-33, pp. 600–607, June 1985.
[8] Ch. E. Tong and R. Blundell, "An annular slot antenna on a dielectric half-space," *IEEE Trans. Antennas Propagat.*, vol. 42, pp. 967–974, July 1994.
[9] J. R. Mosig and F. E. Gardiol, "Rayonnement d'une antenne microruban de forme arbitraire," *Ann. Telecommun.*, vol. 40, nos. 3/4, pp. 1–9, Mar./Apr. 1985.
[10] S. Barkeshli, P. H. Pathak, and M. Marin, "An asymptotic closed-form microstrip surface Green's function for the efficient moment method analysis of mutual coupling in microstrip antennas," *IEEE Trans. Antennas Propagat.*, vol. 38, pp. 1374–1383, Sept. 1990.
[11] M. A. Marin and P. H. Pathak, "An asymptotic closed-form representation for the grounded double-layer surface Green's function," *IEEE Trans. Antennas Propagat.*, vol. 40, pp. 1357–1366, Nov. 1992.
[12] R. L. Rogers and D. P. Neikirk, "Radiation properties of slot and dipole elements on layered substrates," *Int. J. Infrared Millimeter Waves*, vol. 10, no. 6, pp. 697–728, June 1989.
[13] S. M. Wentworth, R. L. Rogers, J. G. Heston, D. P. Neikirk, and T. Itoh, "Millimeter wave twin slot antennas on layered substrates," *Int. J. Infrared Millimeter Waves*, vol. 11, no. 2, pp. 111–131, Feb. 1990.
[14] L. Barlatey, H. Smith, and J. R. Mosig, "Printed radiating structures and transitions in multilayered substrates," *Int. J. Microwave Millimeter-Wave Computer-Aided Eng.*, vol. 2, no. 4, pp. 273–285, Oct. 1992.
[15] J.-M. Laheurte, L. P. B. Katehi, and G. M. Rebeiz, "CPW-fed slot antennas on multilayer dielectric substrates," *IEEE Trans. Antennas Propagat.*, vol. 44, pp. 1102–1111, Aug. 1996.
[16] E. M. Biebl, J. Müller, and H. Ostner, "Analysis of planar millimeter wave slot antennas using a spectral domain approach," in *Proc. IEEE Microwave Theory Tech. Symp. Dig.*, Albuquerque, NM, June 1992, pp. 381–384.
[17] N. Y. Bliznyuk and A. I. Nosich, "Basic properties of the fields excited by VED and HMD located in a dielectric substrate backed by a perfectly conducting ground plane," *Micowave Opt. Technol. Lett.*, vol. 15, no. 5, pp. 316–320, Aug. 1997.
[18] R. F. Harrington, *Time-Harmonic Electromagnetic Fields*. New York: McGraw-Hill, 1961.
[19] J. A. Stratton, *Electromagnetic Theory*. New York: McGraw-Hill, 1941, pp. 34–38.
[20] B. Stockbroeckx, "Space wave and surface wave radiation in the Vivaldi antenna," Ph.D. dissertation, Catholic Univ. Louvain, Louvain-la-Neuve, Belgium, 1998.
[21] V. A. Ditkin and A. P. Prudnikov, *Integral Transforms and Operational Calculus*. London, U.K.: Pergamon, 1965.
[22] M. Abramowitz and I. A. Stegun, *Handbook of Mathematical Functions*. New York: Dover, 1965.
[23] G. N. Watson, *A Treatise on the Theory of Bessel Functions*. London, U.K.: Cambridge Univ. Press, 1966.
[24] A. Sommerfeld, *Partial Differential Equations in Physics*. New York: Academic, 1964.
[25] P. M. Morse and H. Feshbach, *Methods of Theoretical Physics*. New York: McGraw-Hill, 1953.
[26] I. Huynen and B. Stockbroeckx, "Variational principles compete with numerical iterative methods for analyzing distributed electromagnetic structures," in *Proc. Numelec'97*, Lyon, France, 1997, pp. 76–77.
[27] ———, "Variational principles compete with numerical iterative methods for analyzing distributed electromagnetic structures," *Ann. Telecommun.*, vol. 53, nos. 3/4, pp. 95–103, Mar./Apr. 1998.

Benoît Stockbroeckx was born in Brussels, Belgium, in 1970. He received the Engineer (electrical engineering) and Ph.D. (applied sciences) degrees from the Université catholique de Louvain (UCL), Louvain-la-Neuve, Belgium, in 1993 and 1998, respectively.

In 1993, he joined the Microwave Laboratory at UCL. From 1993 to 1994 he investigated ferrite resonators. Since 1994 he has worked on wide-band slotline antenna and Vivaldi antenna modeling. His research interest is in microwave planar circuit modeling.

André Vander Vorst (M'64–SM'68–F'86) was born in Brussels, Belgium, in 1935. He received the Electrical and Mechanical Engineer and Ph.D. degrees in applied sciences from the Université catholique de Louvain (UCL), Belgium, in 1958 and 1965, respectively, and the M.Sc. degree in electrical engineering from the Massachusetts Institute of Technology (MIT), Cambridge, MA, in 1965.

He is associated with UCL, Belgium, where he became an Assistant in 1958, an Assistant Professor in 1962, an Associate Professor in 1968, and a Professor in 1972. From 1958 to 1964, he worked on fast switching of magnetic cores. Under a NATO Fellowship, he was in the U.S. from 1964 to 1966, first at MIT and then at Stanford University, Stanford, CA, both in the field of radio astronomy. In 1966 he founded the Microwave Laboratory at UCL, Belgium, which he still heads. He has been involved in all the research activities of the laboratory, including loaded waveguides and cavities, atmospheric transmission and diffraction up to 300 GHz, designing and measuring active and passive circuits up to and above 100 GHz, and microwave bioelectromagnetics. His current interests are with microwave-optical transducers, humanitarian demining, and the interaction of electromagnetic fields with the nervous system.